# Talbot interferometry with curved quasi-periodic gratings: towards large field of view X-ray phase-contrast imaging

**Yangyang Sun,[1] Wenxiang Cong,[2] Yan Xi,[2] Ge Wang[2] and Shuo Pang [1,*]**

[1]*The College of Optics and Photonics, University of Central Florida, Orlando, FL 32816, USA*
[2]*Department of Biomedical Engineering, Rensselaer Polytechnic Institute, Troy, NY 12180, USA*
*pang@creol.ucf.edu

**Abstract:** X-ray phase-contrast imaging based on grating interferometry has become a common method due to its superior contrast in biological soft tissue imaging. The high sensitivity relies on the high-aspect ratio structures of the planar gratings, which prohibit the large field of view applications with a diverging X-ray source. Curved gratings allow a high X-ray flux for a wider angular range, but the interference fringes are only visible within ~10° range due to the geometrical mismatch with the commonly used flat array detectors. In this paper, we propose a design using a curved quasi-periodic grating for large field of view imaging with a flat detector array. Our scheme is numerically verified in the X-ray regime and experimentally verified in the visible optical regime. The interference fringe pattern is observed over 25°, with less than 10% of decrease in visibility in our experiments.



**OCIS codes:** (070.6760) Talbot and self-imaging effects; (050.0050) Diffraction and gratings; (340.7440) X-ray imaging.

## References and links

1. T. J. Davis, D. Gao, T. E. Gureyev, A. W. Stevenson, and S. W. Wilkins, "Phase-contrast imaging of weakly absorbing materials using hard X-rays," Nature **373**(6515), 595–598 (1995).
2. A. Momose, T. Takeda, Y. Itai, and K. Hirano, "Phase-contrast X-ray computed tomography for observing biological soft tissues," Nat. Med. **2**(4), 473–475 (1996).
3. A. Bravin, J. Keyriläinen, M. Fernández, S. Fiedler, C. Nemoz, M.-L. Karjalainen-Lindsberg, M. Tenhunen, P. Virkkunen, M. Leidenius, K. Smitten, P. Sipilä, and P. Suortti, "High-resolution CT by diffraction-enhanced x-ray imaging: mapping of breast tissue samples and comparison with their histo-pathology," Phys. Med. Biol. **52**(8), 2197–2211 (2007).
4. S. W. Wilkins, T. E. Gureyev, D. Gao, A. Pogany, and A. W. Stevenson, "Phase Contrast Imaging using Polychromatic hard X-rays," Nature **384**(6607), 335–338 (1996).
5. D. Chapman, W. Thomlinson, R. E. Johnston, D. Washburn, E. Pisano, N. Gmür, Z. Zhong, R. Menk, F. Arfelli, and D. Sayers, "Diffraction enhanced x-ray imaging," Phys. Med. Biol. **42**(11), 2015–2025 (1997).
6. F. Pfeiffer, T. Weitkamp, O. Bunk, and C. David, "Phase retrieval and differential phase-contrast imaging with low-brilliance X-ray sources," Nat. Phys. **2**(4), 258–261 (2006).
7. A. Momose, S. Kawamoto, I. Koyama, Y. Hamaishi, K. Takai, and Y. Suzuki, "Demonstration of x-ray Talbot interferometry," Jpn. J. Appl. Phys. **42**(Part 2), L866–L868 (2003).
8. A. Momose, W. Yashiro, K. Kido, J. Kiyohara, C. Makifuchi, T. Ito, S. Nagatsuka, C. Honda, D. Noda, T. Hattori, T. Endo, M. Nagashima, and J. Tanaka, "X-ray phase imaging: from synchrotron to hospital," Philos. Trans. R. Soc., A **372**(2010), 20130023 (2014).
9. J. Tanaka, M. Nagashima, K. Kido, Y. Hoshino, J. Kiyohara, C. Makifuchi, S. Nishino, S. Nagatsuka, and A. Momose, "Cadaveric and in vivo human joint imaging based on differential phase contrast by X-ray Talbot-Lau interferometry," Z. Med. Phys. **23**(3), 222–227 (2013).
10. C. David, J. Bruder, T. Rohbeck, C. Grünzweig, C. Kottler, A. Diaz, O. Bunk, and F. Pfeiffer, "Fabrication of diffraction gratings for hard X-ray phase contrast imaging," Microelectron. Eng. **84**(5-8), 1172–1177 (2007).
11. V. Revol, C. Kottler, R. Kaufmann, I. Jerjen, T. Lüthi, F. Cardot, P. Niedermann, U. Straumann, U. Sennhauser, and C. Urban, "X-ray interferometer with bent gratings: Towards larger fields of view," Nucl. Instrum. Methods Phys. Res., Sect. A **648**, S302–S305 (2011).
12. T. Thüring, "Compact X-ray grating interferometry for phase and dark-field computed tomography in the diagnostic energy range," Diss. Diss., ETH Zürich, Nr. 21321, (2013).

#246751 Received 24 Jul 2015; revised 25 Sep 2015; accepted 27 Sep 2015; published 1 Oct 2015

13. Y. Cohen-Sabban and D. Joyeux, "Aberration-free nonparaxial self-imaging," J. Opt. Soc. Am. **73**(5), 707 (1983).
14. W. D. Montgomery, "Self-Imaging Objects of Infinite Aperture," J. Opt. Soc. Am. **57**(6), 772 (1967).
15. M. Abramowitz, I. A. Stegun, and D. Miller, *Handbook of Mathematical Functions With Formulas, Graphs and Mathematical Tables* (Courier Corporation, 1965).
16. M. V. Berry and S. Klein, "Integer, fractional and fractal Talbot effects," J. Mod. Opt. **43**(10), 2139–2164 (1996).
17. S. Silver and W. K. Saunders, "The external field produced by a slot in an infinite circular cylinder," J. Appl. Phys. **21**(2), 153–158 (1950).
18. J. A. Stratton, *Electromagnetic Theory* (John Wiley & Sons, 2007).

## 1. Introduction

X-ray phase contrast imaging (PCI) can detect small variations of the refractive index, providing superior contrast for low-z elements compared with attenuation contrast [1, 2], and thus is advantageous in imaging biological soft tissues, such as vessels, lesions, and microcalcifications [3]. There are three major imaging methods to retrieve the X-ray phase contrast, namely, propagation-based method [4], analyzer-based method [5] and grating-based method [6, 7]. Compared with the propagation-based method, which requires a high spatial coherent source, and the analyzer-based method, which requires a highly monochromatic X-ray beam, the grating-based PCI system can be implemented by a bench top X-ray source and therefore has great potential for wide-spread applications in medical diagnosis [8, 9].

Standard grating-based PCI system consists of a phase grating G1 and an analyzer grating G2, which are placed between the object and detector, as shown in Fig. 1(a). The flat panel detector is placed immediately after G2. In the case of using an X-ray tube with low spatial coherence, another grating G0 (omitted in the figure) is required between the source and the object [6]. During the imaging process, phase stepping of the analyzer grating G2 is induced, and the information of X-ray attenuation, phase contrast, and small angle scattering can be acquired simultaneously. The PCI sensitivity relies on the frequency of the interference fringes. Flat gratings with high aspect ratio structures are ideal for parallel beams [10]. However, in most non-synchrotron setup, the divergent radiation emerges from the focus of the X-ray tube; therefore, the field of view in the X-ray interferometer is limited to only a few centimeters. The use of a curved phase grating G1 allows perpendicular incidence of X-rays on the gratings, permitting a high X-ray flux with a wider acceptance angle than that associated with a flat grating [11,12]. In these setups, a curved phase grating G1 generates a self-image on a curved analyzer grating G2, posing a geometrical mismatch with a flat panel detector. This mismatch is position dependent and grows nonlinearly as the angle increases. As a result, the mismatch causes a reduction of the visibility of the stepping curve at larger angles and limits the field of view of the curved grating setups. The stepping visibility is defined as ratio between the amplitude and the mean of the phase stepping curve [11].

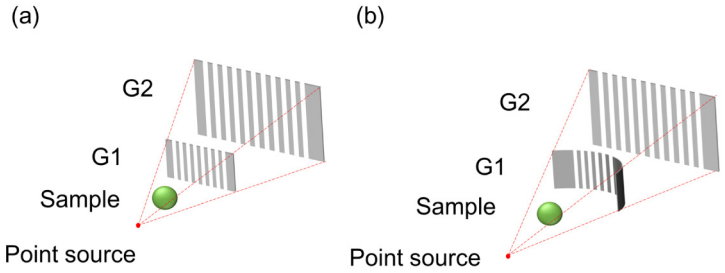


Fig. 1. Setups of grating-based PCI systems. (a) Two flat gratings G1 and G2. (b) A curved phase grating G1 and a flat analyzer grating G2.

In this paper, we propose a curved quasi-periodic phase grating G1' whose self-image occurs on a flat plane, which allows the use of a flat analyzer G2 to match the detector to eliminate the geometric mismatch for a larger field of view in PCI with a flat panel detector,

#246751 Received 24 Jul 2015; revised 25 Sep 2015; accepted 27 Sep 2015; published 1 Oct 2015

as shown in Fig. 1(b). We have experimentally demonstrated a view angle of 25°, with less than 10% of decrease of the visibility of stepping curves, in the visible optical regime. The paper is organized as follows. In Section 2, we present the theory of the self-imaging effect with curved gratings based on scalar diffraction theory and the design method for quasi-periodic gratings. Then, we describe our experimental design and setup in Section 3, followed by the comparison between the analysis and the experimental results in Section 4. Finally, Section 5 concludes our analysis and discusses the similarities and differences between the common X-ray setup and our visible optical experiment.

## 2. Theory

The self-imaging effect of infinite periodic planar structure has been formulated by geometrical ray tracing [13], and scalar diffraction theory under paraxial approximation [14]. In this section, we use an angular decomposition approach similar to [14] to derive the Talbot distance for one dimensional curved gratings in polar coordinates. The analysis is not limited to binary transmission gratings, but also applicable to phase gratings, which are more common as gratings G1 in X-ray PCI setups.

### *2.1 Self-imaging of curved periodic grating*

As depicted in Fig. 1(b), a curved grating G1, whose center is located at the origin of the coordinates system, has a radius of $r_0$. The point source is also placed at the origin. We assume the angular span of the grating is small in the vertical direction, so the irradiance is uniform along the z-axis.

In the case of X-ray PCI setup, the radius of grating G1 (~1 m) is much greater than the period of G1(~1 μm), and the period of G1 is much greater than the wavelength (~0.1 nm), i.e. $r_0 \gg p \gg \lambda$. Under these conditions, a scalar field, $u(\theta, r)$ representing the field after the grating G1 in cylindrical coordinates can be expressed by the sum of the angular Fourier series. The detailed justification of this representation can be found in Appendix A.

$$u(\theta, r) = \sum_{m=-\infty}^{\infty} c_m H_m^{(2)}(kr) \cdot e^{im\theta}, \tag{1}$$

where $r>r_0$, $m$ is an integer representing the angular frequency, $k = 2\pi/\lambda$, is the wave number, $H_m^{(2)}(kr)$ is the Hankel function of second kind representing the outgoing wave, and $c_m$ is the complex coefficient. For $kr \gg m$, the modulus and the phase of $H_m^{(2)}(kr)$ can be expressed asymptotically as [15]:

$$\left|H_m^{(2)}(kr)\right| = \sqrt{\frac{2}{\pi kr} + \mathrm{O}\left(\frac{1}{(\mathrm{kr})^2}\right)}, \tag{2}$$

$$\arg H_m^{(2)}(kr) = -kr + (\frac{1}{2}m + \frac{1}{4})\pi - \frac{4m^2 - 1}{8kr} + \mathrm{O}\left(\frac{1}{(kr)^3}\right). \tag{3}$$

Now we consider the scalar field at the boundary, $r = r_0$, the periodic scalar field can be also be expressed as the sum of its angular Fourier harmonics,

$$u(\theta, r_0) = \sum_{m \in \mathbb{Z}} A_m \cdot e^{im\theta}, \tag{4}$$

where $A_m$ denotes the angular Fourier coefficients. Matching the angular Fourier components of Eq. (1) with Eq. (4) and plugging in the asymptotic expansions in Eq. (2) and Eq. (3), we get

#246751 Received 24 Jul 2015; revised 25 Sep 2015; accepted 27 Sep 2015; published 1 Oct 2015

$$u(\theta,r)=\sqrt{\frac{r_0}{r}}e^{i(kr_0-kr+\frac{1}{8kr}-\frac{1}{8kr_0})}\cdot\sum_{m=-\infty}^{\infty}\left\{e^{i(\frac{m^2}{2k}(\frac{1}{r_0}-\frac{1}{r}))}\right\}\cdot A_m\cdot e^{im\theta}. \tag{5}$$

Equation (5) shows that the amplitude of the field decays as $1/\sqrt{r}$. We can neglect the common phase term outside of the summation operation, since only the phase term, $\exp(im^2(1/r_0-1/r)/2k)$, affects the intensity of the field. In analogy to the infinite periodic planar grating, we consider the case where the circumference of the circle is a multiple of the grating period, and this ratio, $2\pi r_0/p$, is considered as the fundamental angular frequency. Under this condition, the angular Fourier frequency components contain the harmonics of the fundamental angular frequency only, i.e. $m = 2\pi n r_0/p$, where $n$ is an integer. When the field at radius $r_D$, satisfies the equation

$$\frac{1}{r_D}=\frac{1}{r_0}-l\cdot\frac{2p^2}{\lambda r_0^2},l=1,2,3\ldots, \tag{6}$$

the phase term, $\exp(im^2(1/r_0-1/r)/2k)$, is equal to a multiple of $2\pi$ for all the angular frequency $m$, which means that the field $g(\theta, r_D)$ and $g(\theta, r_0)$ have the same intensity distribution along the $\theta$ direction. Equation (6) indicates three facts of the Talbot effect of a curved periodic grating. 1) The self-image is a magnified curved periodic grating sharing the same origin with the original grating G1. 2) The Talbot distance, $r_D - r_0$, has a non-linear relation with $p^2/\lambda$, which is different from the case of planar periodic gratings; 3) there are only a limited number of the self-images, since $l$ is bounded.

*2.2 Quasi-periodic grating*

In the previous subsection, we showed that a curved periodic grating generates a magnified self-imaging grating on a curved plane. In the ideal setup, the analyzer grating G2 is designed so that its period and curvature matches the self-image of G1. However, array detectors with matching curvature are impractical for fabrication. Using a planar analyzer grating G2 and flat detector, depicted in Fig. 1(b), will inevitably result in a loss of the contrast of the stepping curves at large angle.

Motivated by improving the contrast of the stepping curve on a flat detector, we introduce the concept of quasi-periodic gratings to provide one more degree of freedom in the design. Specifically, we perturb the periodicity of the curved grating with a slow-varying term to create a flat self-imaging plane. As shown in Eq. (6), the Talbot distance depends on the grating period $p$. By changing the period along the direction of $\theta$, we can design a quasi-periodic grating having a flat self-image plane. The quasi-periodic grating with slow-varying period can be expressed as:

$$g(\theta,r_0)=\sum_{i\in\mathbb{Z}}rect(\frac{2r_0}{p_i}\theta)*\delta(\theta-\theta_i), \tag{7}$$

where $rect(\cdot)$ denotes the rectangular function, * denotes the convolution operation, and $\delta(\cdot)$ is the Dirac-delta function. $p_i$ denotes the period of the grating at angle $\theta_i$, indexed by $i$. In a strictly periodic grating, $p_i$ is a constant, and $\theta_i = ip_i/r_0$. In a quasi-periodic grating, the angle $\theta_i$ holds the relation with $p_i$,

$$\theta_i=\frac{1}{r_0}(\frac{p_0+p_i}{2}+\sum_{j=1}^{|i-1|}p_j),i=1,2,3..., \tag{8}$$

where $p_0$ denotes the central period of the quasi-periodic grating G1' at $\theta = 0$. The quasi-periodic grating can be treated as local periodic grating for self-imaging, when 1) the amplitude of high harmonic diffraction order is small, $p_i \gg \lambda$, which is satisfied in X-ray PCI

#246751 Received 24 Jul 2015; revised 25 Sep 2015; accepted 27 Sep 2015; published 1 Oct 2015

setups, and 2) the period of the quasi-periodic grating varies slowly. To design a flat self-image plane, the period of the quasi-periodic grating, $p_i$, satisfies the following equation:

$$\frac{2p_i^2}{\lambda r_0^2}+\frac{1}{r_0}=(\frac{2p_0^2}{\lambda r_0^2}+\frac{1}{r_0})\cdot\cos(\theta_i), \tag{9}$$

Using Eq. (8) and Eq. (9), we can calculate the period of the quasi-periodic grating G1' at each angle iteratively.

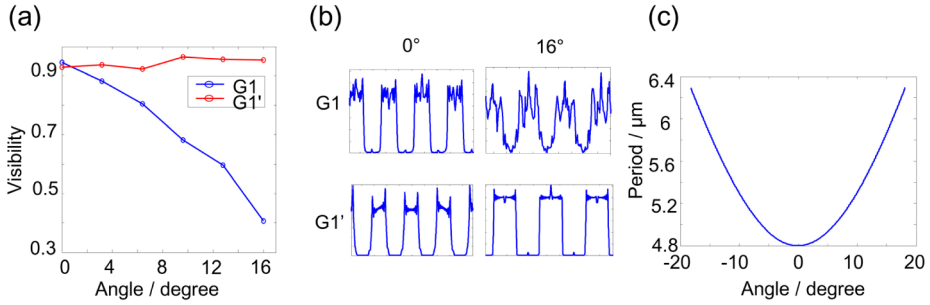


Fig. 2. The simulations in X-ray regime. (a) The visibilities of stepping curves of both G1 and G1'. (b) The intensity profiles at the first fractional Talbot distance of both G1 and G1' at 0° and 16°. (c) The period of the quasi-periodic phase grating G1' as a function of $\theta$.

To demonstrate the performance of the quasi-periodic grating, we conducted numerical simulations with Matlab (Mathwork) for both curved periodic phase grating G1 and quasi-periodic phase grating G1'. In our simulation, the energy of the X-ray beam is 28 keV. We set the period of the phase grating G1 to 4.8 μm, with a radius, $r_0$ = 1.0 m. The center of planar analyzer grating G2 is at the first fractional Talbot image of the center of G1. $1/r_D - 1/r_0 = p^2/8\lambda r_0^2$ [16]. G1' has the central period set to be the same as G1. The calculated period of G1' as a function of $\theta$ is shown in Fig. 2(c), and the period of G2' is calculated accordingly. The period of the quasi-periodic grating is larger than 4.8 μm, and the same fabrication process for periodic grating can be adapted [10]. The pixel size of the detector is set to 24 μm, five times the period of G1. The visibility of the stepping curves at first fractional Talbot distance G1 and G1' are shown in Fig. 2(a). Figure 2(b) shows the intensity profiles of two gratings at 0° and 16°. A decrease of 58% in visibility for G1 at 16° was observed, while no obvious decrease was observed in the visibility for G1'. It is worth noting that the source in the X-ray regime is not a point source. The intensity of a fringe pattern can be expressed as a convolution of the intensity profile of the source and the fringe pattern of an ideal point source. This convolution will decrease the visibility of the fringes pattern. This is always an issue in the X-ray regime to both quasi-periodic and periodic gratings. If necessary, a G0 grating is used for needed spatial coherence.

## 3. Materials and methods

To experimentally verify our analysis, we design the experiments in the visible optical regime. We also conduct the numerical simulation to guide our design. Different from the X-ray simulation, we set G1 as an absorption grating. G2 is separated from G1 by one Talbot distance. The wavelength of the source, $\lambda$, is 0.67 μm to match the optical experiment setup. We set the period of G1, $p_0$, to be 91 μm with a radius, $r_0$ = 75 mm. The quasi-periodic grating G1' has the central period set to be the same as G1. Given that G1' has the same radius as G1, we use Eq. (8) and Eq. (9) to calculate its period $p$ ranging from −30° to 30°. The calculated period of G1' as a function of $\theta$ is shown in Fig. 3(c).

The diagram of the experimental setup is shown in Fig. 4(a). The point source comes from a laser with fiber coupled output (Suprlum, SLD-261, λ = 670 nm). The driven current is set at 133 mA (Suprlum, pilot-2). We use two lenses (f1 = 100 mm, f2 = 62.9 mm) to relay a

#246751 Received 24 Jul 2015; revised 25 Sep 2015; accepted 27 Sep 2015; published 1 Oct 2015

point source to the center of a transparent hollow acrylic tube. The divergence angle of the relayed focal point is 41.0°. The radius of the acrylic tube is 75 mm. Periodic grating and quasi-periodic grating with central period of 91 μm are made on a mylar film with thickness of 180 μm (CAD/Art Services, Inc.), which can be bent easily. Two gratings are taped on the outer surface of the acrylic tube. The detection microscope system includes a microscope objective (Nikon, 10X/0.3), a tube lens (f = 200 mm) and a CMOS camera (JAI, GO5000M), all of which are installed on a motorized translation stage (Thorlab, NRT-100). A stepper motor controller (Thorlab, apt) drives the stage, so that the detection system is able to scan the field in x direction. The scan range of the experiment is 50 mm with 5 mm step size, covering an angular range from −13° to 13°. The microscope objective can adjust its focus in the y direction. The plane with highest fringes contrast near the calculated Talbot distance is set as the observation plane.

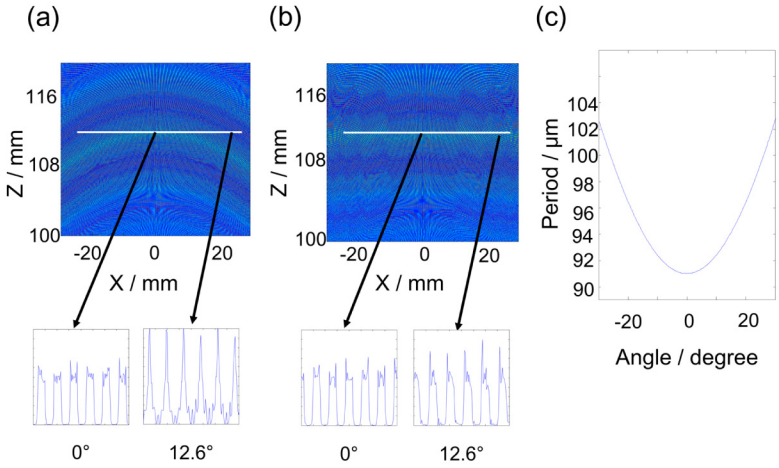


Fig. 3. Simulations in visible optical regime. The wavelength of the source is 0.67 μm. The radius of the grating is 75 mm. The white line, indicating the self-imaging plane, is located at Y = 111.9 mm. (a) The Talbot carpet of the periodic grating G1. The period of the grating is 91 μm. (b) The Talbot carpet of the quasi-periodic grating G1'. The Insert is the line profile of the fields at 0° and 12.6°. (c) The period of the quasi-periodic grating G1' as a function of $\theta$, calculated from Eq. (9).

## 4. Result and discussion

The simulation results in visible optical regime are shown in Figs. 3(a) and 3(b). Figure 3(a) shows the Talbot carpet of the periodic grating G1 in Cartesian coordinates. It can be observed that the self-imaging surface of grating G1 is on a curved plane. Figure 3(b) shows that the self-imaging surface of the quasi-periodic grating G1' is almost flat. The ideal Talbot image is located at $r_D$ = 111.9 mm. If we place a flat array detector at this plane, indicated by the white solid lines in Figs. 3(a) and 3(b), the interference fringes is distorted at 12.6° for periodic grating G1, while the fringes maintain the original fringe profiles for the quasi-periodic grating G1'.

In the optical experiments, we scanned the fields along the x-axis. The images acquired by the CMOS camera at 0°, 7.4°, and 12.2° angles from G1 and G1' are shown in Figs. 4(b)-4(d), respectively. The results also show that the fringes from the periodic grating G1 has a severe distortion at larger angles, while those from the quasi-periodic grating G1' do not change much.

#246751 Received 24 Jul 2015; revised 25 Sep 2015; accepted 27 Sep 2015; published 1 Oct 2015

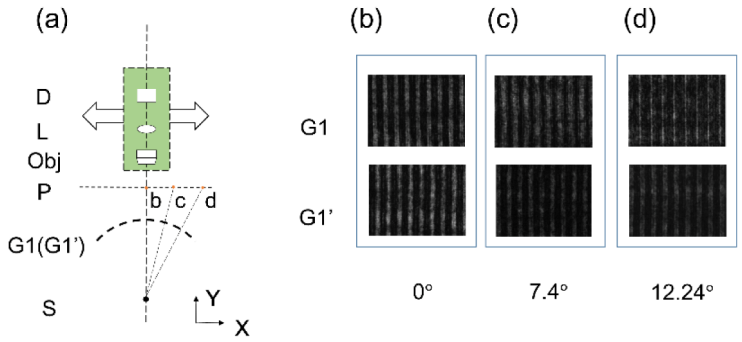


Fig. 4. (a) Experimental setup schematic: S is the point source λ = 0.67 μm, A periodic grating G1 or quasi-periodic grading G1' is fixed on a cylindrical surface. P denotes the observation plane. Obj is the microscope objectives; L is the tube lens; and D is the CMOS detector. (b-d) The images of interference fringes of the observation angles at 0° (b), 7.4° (c), and 12.2°(d) on the observation plane.

In X-ray PCI setups, the pixel size of the detector is ~5 times larger than the period of G1, and the analyzer grating G2 is necessary to resolve the lateral shifts of the fringes. In our experiment, the effective pixel size of CMOS camera after the microscope magnification (~0.5 μm) is less than the period of fringes on observation plane. In order to compare the experimental results, we processed the images to add in a 'virtual' analyzer grating G2. The readout from a virtual pixel consists of five periods of the fringes. Since for quasi-periodic grating the periods have slight variance with respect to the angle, the period of G2' is calculated accordingly at observation plane. The virtue grating G2 and G2' scan 40 phase steps for one period of the fringes. Figure 5 shows the experimental visibility of the periodic grating G1 and quasi-periodic grating G1'. The visibility was calculated from averaging the visibility from 100 sub-regions with 3 mm in width and 2 μm in height on the CMOS camera. We can observe the quasi-periodic grating G1' maintains a uniform visibility on the observation plane. From −13° to 13°, the visibility variance of G1' is less than 10%. While the visibility dropped by 10% for only 5°.

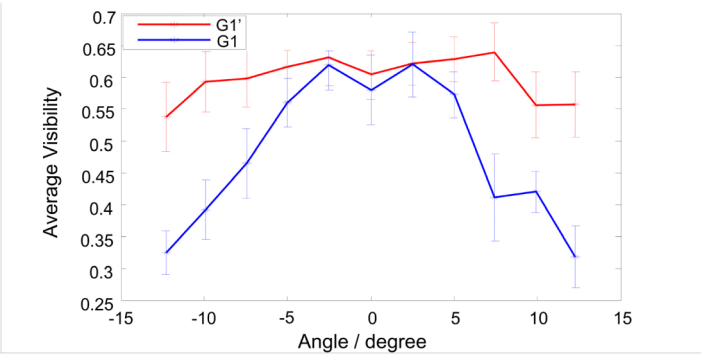


Fig. 5. Experimental data of the visibility with the periodic grating G1 and quasi-periodic grating G1' on the observation plane.

The experimental results have an overall decrease of the visibility. We speculate three reasons causing this difference: the speckle noise, low contrast of the binary mask, and the optical aberration from the mask film.

Firstly, a coherent source is used in the experiment, which introduces laser speckles to the measurement. In addition, the artifacts on the grating surface also contribute to the blur of the interference fringes. From the measured images of the fringes, the average size of the speckles is ~13 μm, and the standard deviation of the intensity is 30%. These artifacts, coupling the

#246751 Received 24 Jul 2015; revised 25 Sep 2015; accepted 27 Sep 2015; published 1 Oct 2015

light to the non-harmonic frequency components of the fringes, can reduce the experimental visibility.

Secondly, the opaque part of the grating is not strictly dark. The opaque region has a measured intensity ~10% of the maximum intensity, which essentially acted as a bias to the field. This low contrast of the grating mask can also decrease the visibility.

Thirdly, due to the mask printing process, the thickness of the transparent region is not uniform. A profilemeter measures the average difference of thickness to be ~0.13 μm. This non-uniform thickness of the mask can introduce a lensing effect. One of the evidences for this speculation is that the field distribution along the Talbot distance is asymmetric. This aberration effect can also affect the visibility.

We incorporated the three aforementioned effects to the simulation. Specifically, to include the speckle noise, we divided the images to small regions with a size of 13 μm, and added random Gaussian noise with a standard deviation of 30% of the local intensity to each region. The transmittance bias and the lensing effect were also included in the simulation. The simulated visibility are shown in Fig. 6 (a). The red point marks the observation plane. The visibility curve, as predicted, is asymmetric from the observation plane. The visibility at the red point is 0.7, which is close to the peak visibility in our experiment. We also measured the intensity pattern at −2 mm, 0 mm and 2 mm away from the observation plane. The experimental images are shown in Fig. 6(b). The simulated and experimental intensity profiles of the interference fringes are shown in Fig. 6(c).

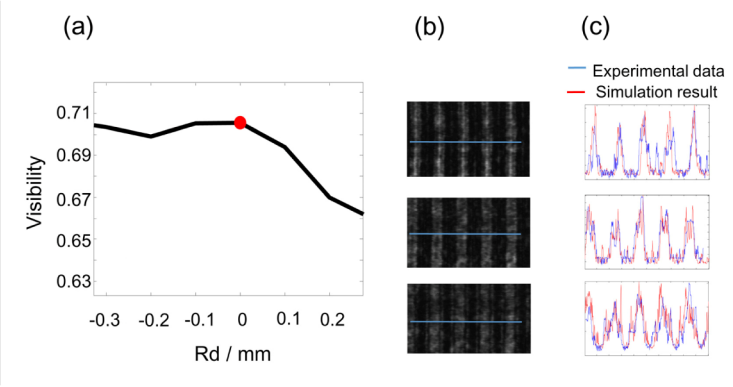


Fig. 6. (a) The simulated visibility profile along the radius direction of the periodic grating, the origin is set at the observation plane. (b) Experimental images of interference fringes at −2 mm, 0 mm, 2 mm from observation plane. (c) Profiles of the interference fringes. Red curves denote simulated profiles. Blue curves denote the gray-scale value profiles of the blue lines marked in 6(b).

It is worth noting that the ratio between the grating period and the wavelength, $p/\lambda$, is on the order of $10^4$ in the X-ray regime, and $p/\lambda$ is on the order of $10^2$ for our experiment in visible wavelength, both of which are sufficiently large for the approximation in Eq. (2) and Eq. (3) to be valid.

## 5. Conclusion

In this paper, we propose a curved quasi-periodic grating for a large field of view X-ray PCI with a flat array detector. In comparison with using a periodic grating G1, a quasi-periodic grating can generate Talbot self-imaging effect on a flat plane, and can thus increase the visibility over a larger range of view angle. We performed the experiment in visible optical regime, and the results support our analysis. We have demonstrated the decrease of the fringe visibility is less than 10% within the view angle of 25°.

The experimental visibility is affected by the speckle noise from the coherent source, the low contrast of the mask transmittance and the optical aberrations from the mask film. We would like to point out that only the low-contrast mask transmittance could reduce the

#246751 Received 24 Jul 2015; revised 25 Sep 2015; accepted 27 Sep 2015; published 1 Oct 2015

visibility of stepping curves in X-ray PCI. The refractive index variance of common materials is much larger in the visible wavelength than that in the X-ray wavelength. The wave front aberration induced by the X-ray grating is almost negligible. We expected that using a quasi-periodic grating could achieve superior results in the X-ray wavelength.

**Appendix A**

In diffraction theory, the vector field can be treated as a scalar field under two conditions: 1) the feature size of the object along the polarization direction of the field are much larger than the wavelength; 2) all components of vector field obey the same scalar wave equation. In general, the second condition is not satisfied in cylindrical coordinates. Here we show that scalar diffraction theory is applicable for the grating analysis for the X-ray PCI imaging.

Under the assumption in Section 2.1, according to [17], The electric field components in free space diffracted by the grating G1 can be expressed as a sum of its Fourier series given by [18]:

$$E_z = \sum_{m\in\mathbb{Z}} a_m H_m^{(2)}(kr)\cdot e^{im\theta}, \tag{10}$$

$$E_\theta = \frac{i\eta_0}{k}\sum_{m\in\mathbb{Z}} b_m \frac{\partial}{\partial r} H_m^{(2)}(kr) e^{im\theta}, \tag{11}$$

$$E_r = \frac{\eta_0 m}{kr}\sum_{m\in\mathbb{Z}} b_m H_m^{(2)}(kr) e^{im\theta}, \tag{12}$$

where $\eta_0 = 1/(\varepsilon_0 c)$, is the impedance of the free space, $k = 2\pi/\lambda$, is the wavenumber, $r>r_0$, $H_m^{(2)}(kr)$ is Hankel function of the second kind representing the outgoing wave, $m$ is integer. For a curved grating with period $p$, $m$ is given by $2n\pi r_0/p$, where $n$ is an integer. In the case of X-ray PCI setup, the radius of grating G1 (~1 m) is much greater than the period of G1(~1 μm), and the period of G1 is much greater than the wavelength (~0.1 nm), i.e. $r_0 \gg p \gg \lambda$. Thus we can use the asymptotic expansions of modulus and the phase of $H_m^{(2)}(kr)$ as in [16]:

$$\left|H_m^{(2)}(kr)\right| = \sqrt{\frac{2}{\pi kr} + \frac{4m^2-1}{2\cdot(2\mathrm{k}r)^2} + \cdots}, \tag{13}$$

$$\arg H_m^{(2)}(kr) = -kr + (\frac{1}{2}m + \frac{1}{4})\pi - \frac{4m^2-1}{8kr} + \frac{(4m^2-1)(4m^2-9)}{6\cdot(4kr)^3} + \cdots, \tag{14}$$

These asymptotic expansions are valid for $kr$ much greater than $m$, i.e. $m/kr \ll 1$. Substituting Eq. (13) and Eq. (14) into Eq. (10), (11) and (12) yields the approximated expressions of the outwardly propagating electric field. Under the condition $r_0 \gg p \gg \lambda$, further approximation can be made as $H'^{(2)}_m/k \approx -i\, H_m^{(2)}$. The three components of the electric field reduce to

$$E_z = \sum_{m\in\mathbb{Z}} a_m H_m^{(2)}(kr)\cdot e^{im\theta}, \tag{15}$$

$$E_\theta = \eta_0 \sum_{m\in Z} b_m H_m^{(2)}(kr)\cdot e^{im\theta}, \tag{16}$$

$$E_r = \frac{m}{kr}\eta_0 \sum_{m\in Z} b_m H_m^{(2)}(kr)\cdot e^{im\theta}, \tag{17}$$

where $r > r_0$, $H_m^{(2)}(kr)$ are approximated by the Eq. (13) and Eq. (14) shows that $E_r$ decays faster along the direction of $r$ than the other two components. Since $m/kr \ll 1$, we have $E_r \ll$

#246751 Received 24 Jul 2015; revised 25 Sep 2015; accepted 27 Sep 2015; published 1 Oct 2015

$E_\theta$. The component $E_r$ can be ignored. The other two components of electric fields have the same form. The components of magnetic field have similar results. Therefore, under the condition $r_0 \gg p \gg \lambda$, all the field components have the same form, and the polarization of the electric field is perpendicular to $r$ direction. Since the two conditions for using scalar diffraction theory are both satisfied, we can use one scalar field $u(\theta, r_0)$ to represent any field component in cylindrical coordinates,

$$u(\theta, r) = \sum_{m \in \mathbb{Z}} c_m \cdot \frac{1}{\sqrt{kr}} e^{-kr + \frac{m}{2} - \frac{4m^2 - 1}{8kr}} \cdot e^{im\theta}, \tag{18}$$

where $c_m$ is the complex Fourier coefficient.

**Acknowledgments**

The authors would like to thank Dr. Aristide Dogariu and Dr. Shintson Wu at University of Central Florida for their help in the experimental setups.

#246751 Received 24 Jul 2015; revised 25 Sep 2015; accepted 27 Sep 2015; published 1 Oct 2015